ChemCatChem

Research Article
doi.org/10.1002/cctc.202401690

Chemistry Europe
European Chemical Societies Publishing

www.chemcatchem.org

Ruthenium-Doped Copper Nanowires for Nitrite/Nitrate to Ammonia Conversion and Their Integration in Zinc–Nitrite Batteries

Tobias Rios-Studer,[a] Zhengfan Chen,[a] Christean Nickel,[a] Fan Feng,[a] Kevin Sowa,[a] Ekemena O. Oseghe,[a] Sina Sadigh Akbari,[a] Sarra Rahali,[a] Leon Prädel,[b] Ingo Lieberwirth,[c] Guangjin Zhang,[d, e, f] Dandan Gao,*[a] Rongji Liu,*[a] and Carsten Streb*[a]

The electrochemical reduction of nitrite (NO_2^-) and nitrate (NO_3^-) not only enables sustainable, circular routes to produce ammonia (NH_3), but also eliminates pollutants in groundwater. In this article, we report a facile synthesis of Ru-doped Cu nanowires on Cu foam electrodes with low Ru (0.48 wt.%) loading. The composite electrode shows high-performance in the NO_2^-/NO_3^- to NH_3 electroreduction, giving NH_3 Faradaic efficiency of up to 100% and NH_3 yield rates up to 33.2 mg h^{-1} cm^{-2} at −0.2 V versus RHE in NO_2^- reduction. For the nitrate-to-ammonia reduction, the electrode also shows high activity with Faradaic efficiency of 88.4% (at −0.6 V versus RHE) and a yield rate of 62.5 mg h^{-1} cm^{-2} (at −1.0 V versus RHE). We show that the electrode can easily be integrated into a Zn–nitrite battery, giving a power density of 9.1 mW cm^{-2}, a NH_3 yield rate of 1.88 mg h^{-1} cm^{-2} and a nitrite-to-ammonia Faradaic efficiency of 88.9% at a current density of 20 mA cm^{-2}. The system combines three productive outputs, that is removal of NO_x^- pollutants, synthesis of valuable NH_3 and generation of "green" electricity.

1. Introduction

Ammonia (NH_3) is one of the most essential and important chemical feedstocks in modern society, with over 150 million tons produced annually. NH_3 plays a crucial role in the production of nitrogen fertilizers for agriculture and many chemicals for industry.[1–3] Additionally, NH_3 is gaining increasing interest as carbon-free fuel for energy storage due to its high energy density (4.3 kWh kg^{-1}).[4] To-date, the Haber–Bosch-process is the dominant route in the synthesis of NH_3, where NH_3 is formed by the reaction of gaseous nitrogen (N_2) with gaseous hydrogen (H_2) under high temperature and high pressure, which results in a high energy demand and a significant impact on the global carbon footprint. The Haber-Bosch-process consumes about 1–2% of all energy worldwide and is responsible for more than 1%of the annual global CO_2 emissions.[5,6] To solve this problem, electrochemical synthesis of NH_3 under ambient conditions offers an energy-efficient reaction pathway.[7,8] However, the direct reduction of nitrogen comes with challenges, such as the low aqueous solubility and high dissociation energy. Furthermore, the potential needed to reduce nitrogen is in a region where the hydrogen evolution reaction (HER) occurs. An alternative to the reduction of nitrogen is the reduction of NO_x^- (nitrate (NO_3^-) and nitrite (NO_2^-)), which is easily dissolved in water and the dissociation energy of the N=O bond (204 kJ mol^{-1}) is only about a quarter of the dissociation energy of the N_2 triple bond (941 kJ mol^{-1}).[9] NO_x^- is also a major water pollutant due to extensive fertiliser use and industrial processes, and its accumulation in the environment leads to serious health and ecological issues.[10] The urgent need to eliminate NO_x^- and produce NH_3 makes the NO_x^- reduction reaction (NO_xRR) via an efficient electrocatalytic route particularly compelling.[1,11,12]

Although electrocatalytic NO_xRR has garnered increasing attention from researchers as a promising pathway for NH_3 synthesis, the reaction kinetics and product selectivity in electrochemical NO_xRR are largely determined by the choice of catalyst.

[a] T. Rios-Studer, Z. Chen, C. Nickel, F. Feng, K. Sowa, Dr. E. O. Oseghe, Dr. S. S. Akbari, S. Rahali, Dr. D. Gao, Dr. R. Liu, Dr. C. Streb
Department of Chemistry, Johannes Gutenberg University Mainz, Duesbergweg 10–14, Mainz 55128, Germany
E-mail: dandan.gao@uni-mainz.de
rongji.liu@uni-mainz.de
carsten.streb@uni-mainz.de

[b] L. Prädel
Department for Molecular Spectroscopy, Max Planck Institute for Polymer Research, Ackermannweg 10, Mainz 55128, Germany

[c] Dr. I. Lieberwirth
Department of Physical Chemistry of Polymers, Max Planck Institute for Polymer Research, Ackermannweg 10, Mainz 55128, Germany

[d] G. Zhang
Center of Materials Science and Optoelectronics Engineering, Chinese Academy of Sciences, Beijing 100049, PR China

[e] G. Zhang
CAS Key Laboratory of Green Process and Engineering, Institute of Process Engineering, Chinese Academy of Sciences, Beijing 100190, PR China

[f] G. Zhang
Key Laboratory of Green and High-value Utilization of Salt Lake Resources, Chinese Academy of Sciences, Beijing 100190, PR China

Supporting information for this article is available on the WWW under https://doi.org/10.1002/cctc.202401690

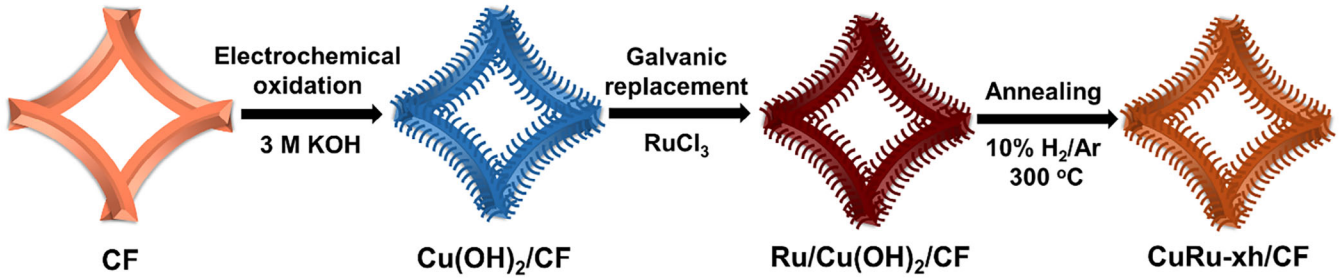

Scheme 1. Schematic illustration of the synthetic process of CuRu-xh/CF.

To date, a wide range of catalysts have been reported in recent years such as noble metals,[13–15] transition metals,[16,17] metal alloys,[18–25] as well as metal oxides.[26–28] Among them, Cu-based materials have emerged as particularly attractive candidates for NO_xRR due to their low cost, weak hydrogen evolution tendency, and high electrical conductivity.[17,19,29–33] However, the weak adsorption of hydrogen (H_{ad}) on bare Cu limits the hydrogenation rate of N-intermediates, resulting in low Faradaic efficiency (FE) for NH_3 production. To address this issue, noble metals such as Rh, Ru, Pt, and Au, known for their excellent hydrogen adsorption–desorption properties, have been merged with Cu substrates to enhance the hydrogenation ability of Cu-based catalysts at more positive potentials, significantly reducing the overpotential for the NO_xRR.[25,34] It has been proposed that the Cu site preferentially stabilizes nitrogen intermediate species, whereas the vicinal noble metals supply the activated H species required for the surface hydrogenation to proceed. Additionally, due to synergistic effects, 3d transition metals like Fe, Co, and Ni have also been used to modify Cu-based electrodes to create bimetallic composite materials with high NO_xRR performance.[35]

This report builds on pioneering work on the design of noble metal (Ru and Rh)-doped nanostructured Cu catalysts.[25,34] Here, we used a modified method for synthesizing a Cu foam (CF) based composite electrode, where Cu nanowires were grown on the CF surface, and Ru sites where then deposited on the Cu nanowires. The resulting composite is referred to as CuRu-xh/CF, where x represents the duration of the galvanic replacement reaction. The catalyst shows high selectivity towards NH_3 formation and inertness toward HER, as well as a low NO_2^- activation barrier reported for Ru catalysts.[34,36] The optimized electrode CuRu-3 h/CF shows high performance for both, nitrite and nitrate reduction to ammonia, and integration into an aqueous zinc–nitrite battery demonstrated the technological deployment of the system.

2. Results and Discussion

Scheme 1 shows the three-step synthetic process for CuRu-xh/CF (see details in the experimental procedures in Supporting Information). Briefly, the CF was firstly electrochemically oxidised to $Cu(OH)_2$/CF, the obtained $Cu(OH)_2$/CF was then treated with $RuCl_3$ solution in a galvanic replacement reaction to obtain $Ru/Cu(OH)_2$/CF. In the last step, the $Ru/Cu(OH)_2$/CF was annealed in a 10% H_2/Ar atmosphere to obtain CuRu-xh/CF. The electrodes were used as-prepared without further pretreatment.

Powder X-ray diffraction (pXRD) was used to confirm the formation of $Cu(OH)_2$ during the electrochemical oxidation (Figure S1). The pXRD patterns of pure CF, as well as the synthesized pure nanostructured CF (NCF, see experimental procedures in Supporting Information) and CuRu-xh/CF, are compared in Figure 1a. The pure CF as well as the synthesized electrodes exhibit three distinct diffraction peaks at two theta values of 43.3°, 50.4°, and 74.1°, which are attributed to the (111), (200) and (220) lattice planes of a face centred cubic (fcc) crystalline structure of Cu (PDF#70–3039). However, no diffraction peaks associated with metallic Ru were present in CuRu-xh/CF, which indicates that no crystalline Ru particles are present.[37]

X-ray photoelectron spectroscopy (XPS) analyses reveal the presence of both Cu and Ru in CuRu-3 h/CF. The high-resolution Cu 2p XPS spectrum of CuRu-3 h/CF is shown in Figure 1b. The spectrum shows strong peaks of Cu^0 $2p_{3/2}$ and Cu^0 $2p_{1/2}$ located at binding energies of 932.5 eV and 952.2 eV as well as weak peaks at higher binding energies of 934.1 eV and 954.2 eV associated with Cu^{2+}.[38] To distinguish the chemical states between copper metal and oxides, we have also performed Cu Auger XPS analysis. The Cu LMM Auger spectrum of CuRu-3 h/CF (Figure S2a, Supporting Information) shows the peaks associated with Cu^{2+}, Cu^+ and Cu^0[39–41] indicating the partial surface oxidation of metallic Cu in CuRu-3 h/CF. Figure 1c displays the high-resolution Ru 3d XPS spectrum of CuRu-3 h/CF. Similarly, the peaks could be deconvoluted into separated peaks for both Ru^0 and Ru^{4+}.[42] Besides, the high-resolution Ru 3p XPS spectrum (Figure S2b, Supporting Information) also shows the peaks associated with both Ru^0 and Ru^{4+},[43] which could also indicate the partial surface oxidation of metallic Ru in CuRu-3 h/CF.

The morphology of the different electrodes was investigated using scanning electron microscopy (SEM). The surface of the pure CF is smooth (Figure S3), whereas the images of $Cu(OH)_2$/CF (Figure S4) show a change of the morphology to a uniform nanowire structure during the electrochemical oxidation, where the nanowires appear smooth and straight. After galvanic replacement and annealing, the nanowires shown in the images of CuRu-xh/CF are no longer smooth and straight and instead appear elongated and curved with many particles agglomerated on the nanowires (Figure 1d,e and Figures S5–S7, Supporting Information). This structural change is also present in NCF (Figure S8), which was prepared without the galvanic replacement reaction, indicating the aggregation of metallic Cu nanoparticles on the nanowires during the thermal reduction of $Cu(OH)_2$. The comparison indicates that the structural

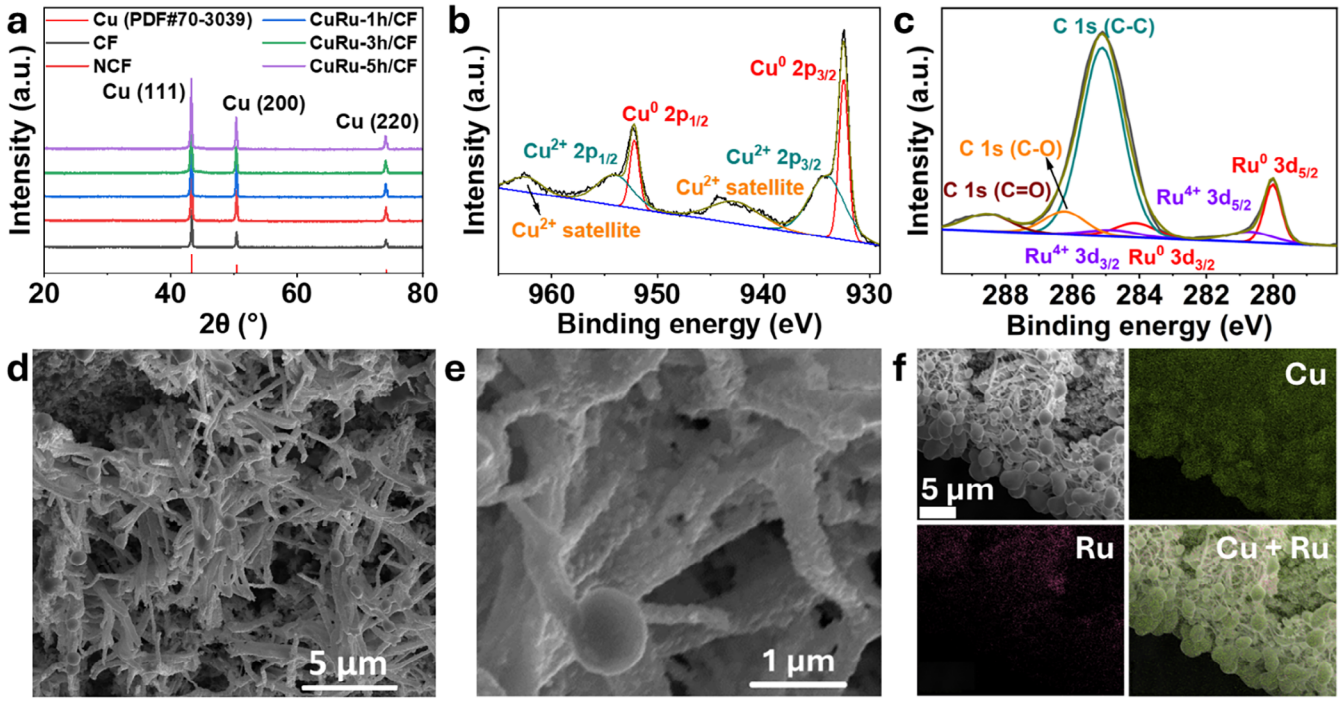

Figure 1. Structural and elemental analyses of CuRu-xh/CF. (a) pXRD pattern of the synthesized electrodes. (b) High-resolution Cu 2p XPS spectrum. (c) High-resolution Ru 3d XPS spectrum of CuRu-3 h/CF. (d and e) SEM images of CuRu-3 h/CF with different magnifications. (f) SEM-EDX elemental mapping of CuRu-3 h/CF.

changes occur during the annealing process, not during the cation exchange process. However, it should be noted that the duration of the galvanic replacement reaction affects the morphology. By comparing the different CuRu-xh/CF electrodes, it can be observed that a shorter reaction time (CuRu-1 h/CF and CuRu-3 h/CF) does not lead to significant changes in morphology. However, some particle aggregation is noticeable at the ends of the nanowires (Figure 1d,e and Figures S5 and S6, Supporting Information). If the galvanic replacement reaction time was extended to 5 h, the nanowires were no longer uniformly present on the surface, and instead were agglomerated (Figure S7). SEM energy dispersive X-ray spectroscopy (SEM-EDX, Figure 1f and Figure S9, Supporting Information) shows that Ru is uniformly distributed on the Cu surface. The loading of Ru determined by inductively coupled plasma optical emission spectroscopy (ICP-OES) for CuRu-xh/CF was 0.25 wt.% ($x = 1$), 0.48 wt.% ($x = 3$) and 0.92 wt.% ($x = 5$) respectively (Figure S10, Supporting Information). This indicates prolonged galvanic replacement time can be used to control the Ru loading amount. Furthermore, we have also performed transmission electron microscopy (TEM) and high-resolution TEM (HRTEM) to get more detailed information about the CuRu-3 h/CF electrode (Figure S11, Supporting Information). The images of the surface layer of the electrode show a polymorphic structure. The lattice spacing was determined as 0.30 nm which corresponds to the lattice spacing of Cu_2O (110) (Figure S11d,e), which further indicates partial surface oxidation of CuRu-3 h/CF electrode.

The NO_2RR performance was tested in an H-cell filled with 1 M aqueous KOH as electrolyte, the two cell compartments were separated by a Nafion 117 membrane. A three-electrode system using the as-prepared CF-based electrode as the working electrode, Hg/HgO (1 M KOH) as the reference electrode and the Pt wire as the counter electrode. All potentials reported in this study were converted to reversible hydrogen electrode potentials (RHE).

To gain fundamental insight into the electrode reactivity, we performed linear scan voltammetry (LSV) of the pure CF, NCF, and CuRu-xh/CF electrodes between 0.6 and −0.6 V versus RHE in the presence and absence of 0.1 M $NaNO_2$. As shown in Figure 2a, the current density for all electrodes increased over a wide range of potentials in the presence of NO_2^-, compared to the LSV performed without NO_2^-, which indicates the apparent reduction of NO_2^- for all these electrodes. The reduction peak at ~0.4 V can be attributed to the reduction of Cu^{2+} to Cu^+.[44,45] Further comparison indicates that the presence of nanowire structure of the synthesized electrodes resulted in a higher catalytic activity compared to pure CF that was further increased in the presence of Ru (CuRu-xh/CF). CuRu-3 h/CF shows the highest catalytic activity and the current density reaches 570 mA/cm^2 at a potential of −0.6 V versus RHE. Additionally, CuRu-xh/CF shows a lower onset potential for NO_2^- reduction at 0.25 V versus RHE, compared to pure CF (−0.05 V versus RHE). We further performed the Tafel slope analysis of different electrodes toward NO_2RR (Figure S12, Supporting Information). It is shown that the Tafel slope of NCF (152 mV dec^{-1}) significantly decreased compared with that of CF (207 mV dec^{-1}) due to the formation of nanowires on the surface of NCF. While the doping of Ru on the NCF (CuRu-xh/CF electrodes) further increased the Tafel slopes that could be due to the different reaction mechanisms caused by the interaction between Ru and Cu. However, due to the

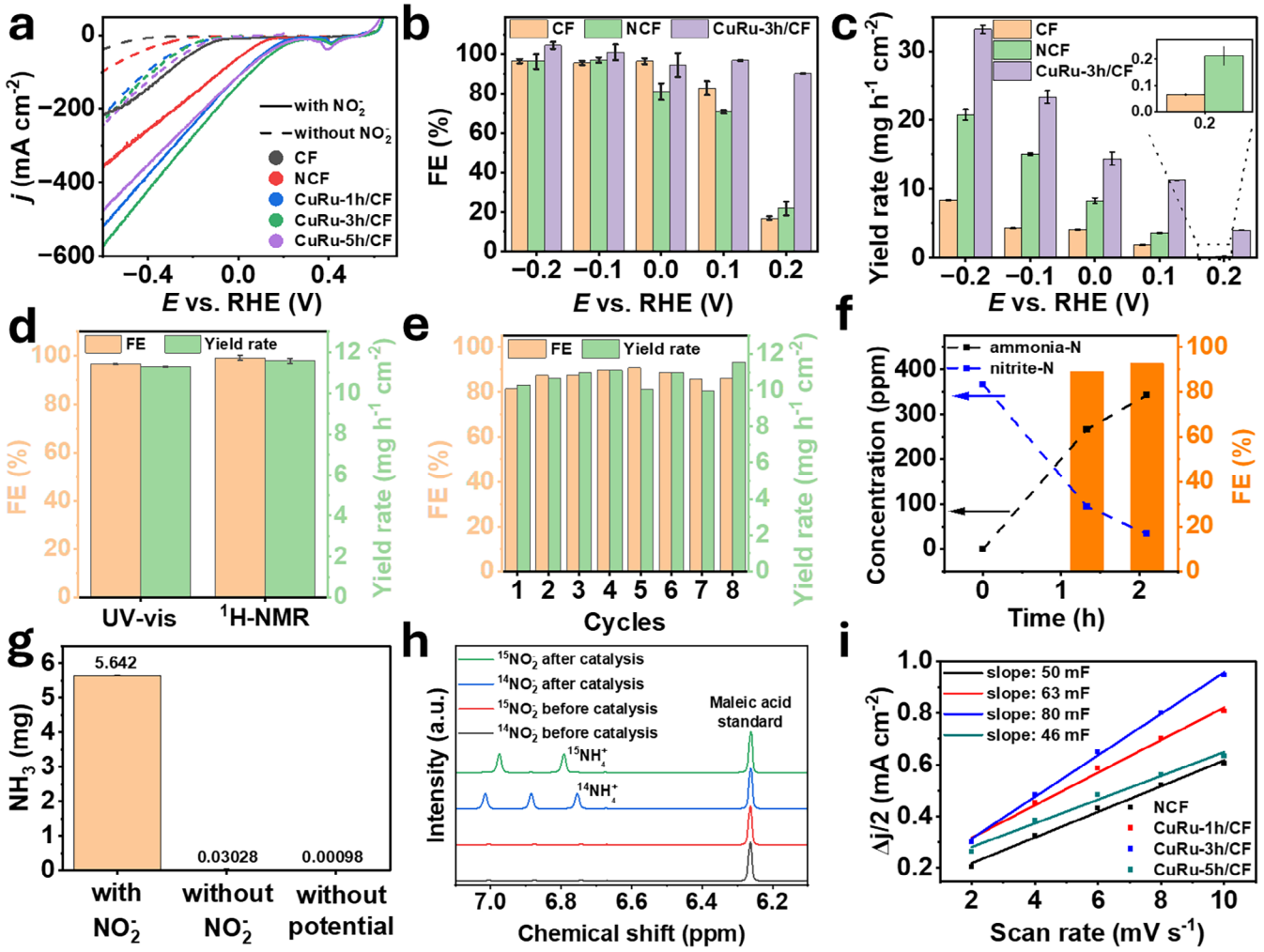

Figure 2. Electrocatalytic NO_2RR performance of different electrodes in 1 M KOH solution. (a) LSV curves of pure CF, NCF, and CuRu-xh/CF in the presence and absence of NO_2^-. (b) NH_3 FE and (c) NH_3 yield rate of pure CF, NCF, and CuRu-3 h/CF. The error bars represent the standard deviations of three independent measurements. (d) Nitrite-to-NH_3 FE and yield rate of CuRu-3 h/CF at 0.1 V versus RHE, detected by indophenol blue method and ^1H NMR spectroscopy. (e) Cycling stability tests of CuRu-3 h/CF at 0.1 V versus RHE. (f) NO_2^- removal using CuRu-3 h/CF with an initial nitrite-N concentration of 365 ppm at a potential of −0.2 V versus RHE. (g) NH_3 yield of CuRu-3 h/CF with NO_2^- at 0.1 V versus RHE, without NO_2^- at 0.1 V versus RHE and without potential in the presence of NO_2^-. (h) ^1H NMR spectra of the electrolyte before and after electrocatalysis using $^{14}NO_2^-$ and $^{15}NO_2^-$ as nitrogen source. (i) ECSA analysis of NCF and CuRu-xh/CF.

potential coexistence of both HER and NO_2RR, and the complex multistep NO_2RR process, it is not easy to investigate the kinetics of NO_2RR by using simple Tafel slope analysis.

Thereafter, chronoamperometry tests were performed at potentials between 0.2 and −0.2 V versus RHE to determine NH_3 selectivity of the NO_2RR using pure CF, NCFand CuRu-3 h/CF as catalysts (Figure S13, Supporting Information). We used the indophenol blue method (IBM) with UV–vis absorption spectroscopy as well as ^1H NMR spectroscopy to confirm and quantify the NH_3 production at different potentials (Figure S14, Supporting Information).[46] The resulting potential dependent NH_3 FE is shown in Figure 2b. It can be seen that the FE of CuRu-3 h/CF is the highest at all applied potentials and reaches ~100% even at a positive potential of 0.1 V versus RHE. It is notable that the nanostructured NCF does not result in a higher FE than pure CF, indicating the presence of Ru in CuRu-3 h/CF is the cause of the notably higher selectivity towards NH_3 formation. The corresponding NH_3 yield rates are shown in Figure 2c. It is visible that CuRu-3 h/CF also shows the highest yield rate at all applied potentials with a maximum yield rate of 33.2 mg h^{-1} cm^{-2} at a potential of −0.2 V versus RHE, which is about four times higher than that of pure CF. It should be noted that NCF shows a notably higher yield rate than pure CF, suggesting that the Cu nanowire structure in NCF enhances catalytic activity compared to the smooth surface of pure CF, most likely due to the increased specific surface area. We also compared the calculated FE and yield rate of NH_3 measured by IBM and NMR spectroscopy. As shown in Figure 2d, the results of the two different methods are consistent. Next, we tested the long-term stability of the CuRu-3 h/CF catalyst using eight consecutive 30-min electrolysis cycles at 0.1 V versus RHE (Figure S15, Supporting Information). The NH_3 yield rate and FE of each cycle are shown in Figure 2e. It is shown that the NH_3 yield rate and FE were essentially maintained over 8 cycles, indicating the CuRu-

3 h/CF has a high stability for the NO_2RR. Post-catalytic analysis of CuRu-3 h/CF gave us further information regarding the structural stability. The pXRD patterns show that there is no change in structure and the same diffraction peaks are present after the reaction (Figure S16, Supporting Information). Cu LMM Auger XPS analysis of Cu shows a decrease of Cu^{2+} and increase of Cu^{+} after the reaction (Figure S2a,c, Supporting Information), indicating the partial surface reduction during NO_2RR. The high-resolution Ru 3p XPS spectrum after the reaction does not show any Ru signal (Figure S2d, Supporting Information). However, ICP-OES was used to verify the presence of Ru, and the loading amount of Ru after reaction was ~0.29 wt.%, indicating some leakage of Ru during reaction. Encouragingly, the leaking of Ru did not reduce much of the activity of the CuRu-3 h/CF electrode. SEM images (Figure S17, Supporting Information) of CuRu-3 h/CF after NO_2RR indicate that the surface structure changed from nanowires to nanosheets during the reaction. SEM-EDX analyses show that Ru is still uniformly distributed on the surface after the reaction (Figures S18 and S19, Supporting Information). However, we note that this surface restructuring of CuRu-3 h/CF does not have a significant effect on the NO_2RR activity of this material.

To investigate the NO_2^- removal capabilities of CuRu-3 h/CF, a batch conversion test was performed at −0.2 V versus RHE with a nitrite-N concentration of 365 ppm (Figure 2f). NO_2^- quantification was determined using *N*-(1-naphthyl)ethylene diamine spectrophotometric method (Figure S20, Supporting Information).[47] Even at this low nitrite concentration, the nitrite-to-ammonia FE reached 92%. After 2 h of electrolysis, only 9% of the initial nitrite concentration (i.e., 33 ppm remained in the solution. Note that the sum concentrations of nitrite-N and ammonia-N throughout the measurement remain constant and are consistent with the initial nitrite-N concentration, indicating the high NO_2^- to NH_3 conversion selectivity. Even at a positive potential of 0.1 V versus RHE, the CuRu-3 h/CF still shows efficient conversion of NO_2^- to NH_3. The FE reached as high as 92% after 2 h electrolysis and remained above 80% after 6 h, with only 5% of the initial nitrite (with a nitrite-N concentration of 19 ppm) remaining in the solution at the end (Figure S21).

To confirm the origin of the nitrogen atoms incorporated in the synthesized NH_3, several control experiments were undertaken. First, we note that virtually no NH_3 is detected when 0.1 M aqueous NO_2^- solutions were kept at the open circuit potential (OCP). Also, when a potential of 0.1 V versus RHE was applied, no significant NH_3 formation was detected unless NO_2^- was present in the solution (Figure 2g). These results indicate that NH_3 originated from the reduction of NO_2^-. Also, isotope labelling experiments were carried out for NO_2RR in the presence of $^{14}NO_2^-$ or $^{15}NO_2^-$ followed by product identification and quantifications via ^1H NMR. As shown in Figure 2h, the characteristic splitting of the ^1H resonance into 3 symmetric signals when using $^{14}NO_2^-$ and the corresponding splitting into 2 symmetric signals when using $^{15}NO_2^-$ reveal the presence of $^{14}NH_4^+$ and $^{15}NH_4^+$ in the NMR spectra. The above results verify that NH_3 originates from NO_2^- reduction.

To understand the origin of the notable NO_2RR performance of CuRu-3 h/CF, we measured the electrochemically active surface area (ECSA) and the charge-transfer resistance (R_{ct}) at the electrode/electrolyte interface, as both parameters are crucial for the reactivity of heterogeneous electrocatalysts. Electrochemical double-layer capacitance (C_{dl}) tests were performed to determine the ECSA of the synthesized CF-based electrodes (Figures S22 and S23, Supporting Information). Figure 2i shows the C_{dl} of the electrodes, the resulting ECSA is shown in Figure S24, Supporting Information. It is noted that CuRu-3 h/CF shows the highest ECSA among all the electrodes. The result shows that the addition of Ru first leads to an increase in ECSA compared to NCF, but longer reaction time in CuRu-5 h/CF leads to a decrease in ECSA, which may be attributed to the agglomeration of the Cu nanowires as observed from the SEM images. Further, an electrochemical impedance study (EIS) was performed to determine the R_{ct} of the electrodes (Figure S25, Supporting Information). It is notable that CuRu-3 h/CF features more than ten times lower R_{ct} than that of NCF, which enables efficient and fast electron transfer at the solid–electrolyte interface, whereas all the CuRu-xh/CF electrodes have similar R_{ct} values (Table S1, Supporting Information). These specific characteristics grant CuRu-3 h/CF its superior activity for NO_2RR.

Furthermore, we also investigated the performance of CuRu-3 h/CF in NO_3RR. First, we performed LSV between 0.6 V and −1.2 V versus RHE in the presence and absence of NO_3^- (Figure S26, Supporting Information). The current density increases with more negative potentials in the presence of NO_3^-, indicating the efficient reduction of NO_3^-. Next, we performed CA measurements at potentials between −0.1 and −1.0 V versus RHE (Figure S27, Supporting Information). The NH_3 production was confirmed and quantified using the IBM, and the resulting nitrate-to-ammonia FE and yield rate are displayed in Figure S28, Supporting Information. Highest FE (88.4%) was detected at a potential of −0.6 V versus RHE; the highest yield rate (62.5 mg h^{-1} cm^{-2}) was observed at −1.0 V versus RHE. The above results show that CuRu-3 h/CF has high performance for the conversion of NO_x^- to NH_3, which is comparable to the related CF-based catalysts (Tables S2 and S3, Supporting Information).

For a practical application, we designed a zinc–nitrite battery using CuRu-3 h/CF as cathode and zinc foil as anode (Figure 3a). The battery maintains a constant OCP of 1.13 V for at least 6 h (Figure 3b). Figure 3c shows the charge-discharge LSV curves of the CuRu-3 h/CF based zinc–nitrite battery. The discharge curve shows an increasing output current density with more negative cathodic potential, and the power density reaches 9.1 mW cm^{-2}. The time dependent discharge curves of the battery at current densities from 2 to 30 mA cm^{-2}, displayed in Figure 3d, indicate a good long-term electrochemical stability. Figure 3e displays the NH_3 yield and corresponding FE during discharge with various output current densities. The CuRu-3 h/CF based zinc–nitrite battery achieves a NH_3 yield rate of 1.88 mg h^{-1} cm^{-2} and a FE of 88.9% at a current density of 20 mA cm^{-2}. Lastly, the CuRu-3 h/CF based zinc–nitrite battery was used to power an electronic timer for at least 18 h (Figure 3f). In summary, the Zn-nitrite battery achieves three tasks: sustainable energy supply, NH_3 electrosynthesis and removal of NO_2^- pollutant in wastewater.[48,49]

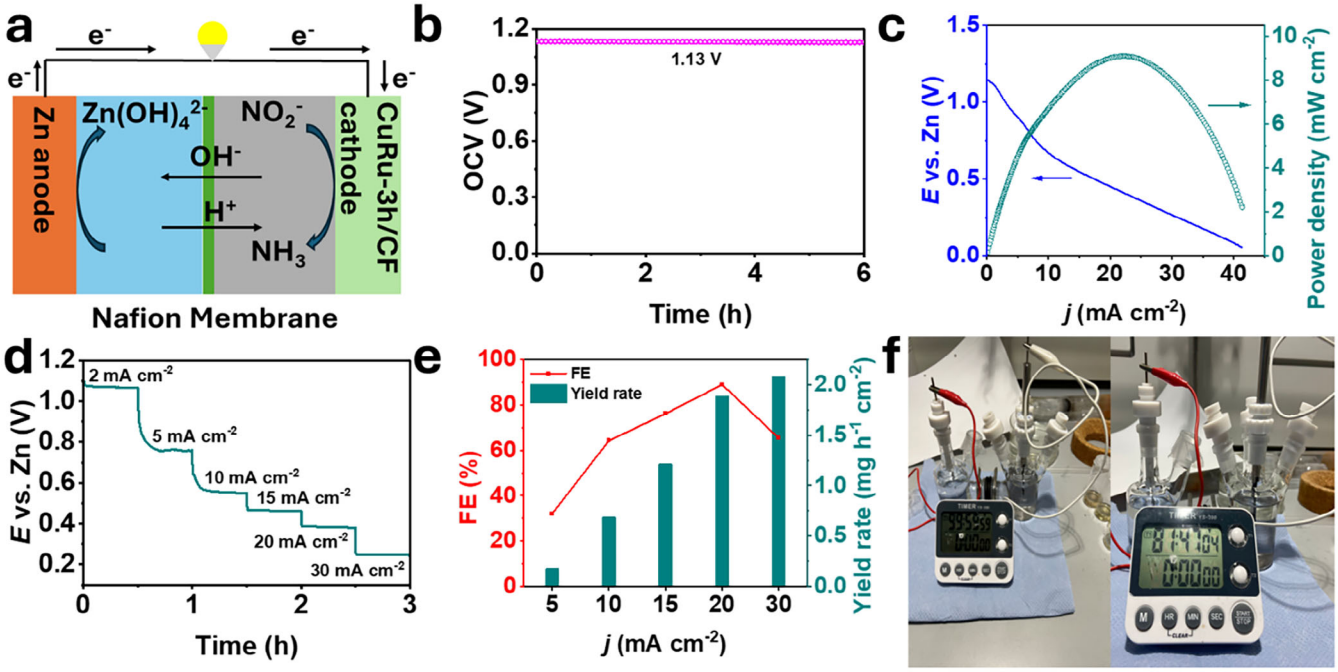

Figure 3. Zinc–nitrite battery test. (a) Schematic illustration of the zinc–nitrite battery with Zn anode and CuRu-3 h/CF cathode. (b) Open-circuit voltage of the zinc–nitrite battery. (c) Discharge polarisation curve and corresponding power density curve of the zinc–nitrite battery. (d) Discharging curves at different current densities. (e) NH_3 FE and yield rate of the zinc–nitrite battery. (f) Photograph of an electronic timer powered by our CuRu-3 h/CF based zinc–nitrite battery.

3. Conclusion

In summary, we report the facile synthesis of a Ru-doped Cu nanowires electrode for highly efficient NO_{x^-} to $-NH_3$ reduction with high activity (with FE near 100% and a yield rate of 33.2 mg h^{-1} cm^{-2} at a potential of −0.2 V versus RHE) and high stability. Integration of the electrode into a Zn-nitrite battery demonstrated its operational capacity for combined sustainable electricity production, NH_3 electrosynthesis, and NO_2^- pollutant removal. The reported approach provides us a hint for designing high-performance transition metal-based catalysts for sustainable NH_3 synthesis.

Supporting Information

Experimental and analytical data are available as Supporting Information. The raw data reported in this manuscript is available at zenodo.org via https://doi.org/10.5281/zenodo.13881049.

Acknowledgements

The authors gratefully acknowledge financial support by the Deutsche Forschungsgemeinschaft DFG (SPP 2370 Nitroconversion, project no. 501934135, and TRR 234 CataLight, project number: 364549901). Ekemena O. Oseghe, Sina Sadigh Akbari, Sarra Rahali, and Rongji Liu gratefully acknowledge financial support by the Alexander von Humboldt Foundation. Dandan Gao acknowledges the Deutsche Forschungsgemeinschaft (DFG) for a Walter Benjamin Fellowship (project no. 510966757). Guangjin Zhang and Carsten Streb acknowledge the International CAS Partnership Project (039GJHZ2022029GC). Rongji Liu, Dandan Gao, and Carsten Streb gratefully acknowledge financial support by Johannes Gutenberg University Mainz, the Top-Level Research Initiative SusInnoScience, and the Gutenberg Research College. The authors acknowledge Dr. Mihail Mondeshki for NMR measurements and discussion.

Open access funding enabled and organized by Projekt DEAL.

Data Availability Statement

The data that support the findings of this study are openly available in zenodo.org at https://doi.org/10.5281/zenodo.13881049, reference number 13881049.

Keywords: Ammonia synthesis · Electrocatalysis · Nitrate reduction · Nitrite reduction · Zn-nitrite batteries

[1] P. H. van Langevelde, I. Katsounaros, M. T. M. Koper, *Joule* **2021**, *5*, 290–294.
[2] H. Xu, Y. Ma, J. Chen, W. X. Zhang, J. Yang, *Chem. Soc. Rev.* **2022**, *51*, 2710–2758.
[3] C. J. M. Van Der Ham, M. T. M. Koper, D. G. H. Hetterscheid, *Chem. Soc. Rev.* **2014**, *43*, 5183–5191.
[4] E. Spatolisano, L. A. Pellegrini, A. R. de Angelis, S. Cattaneo, E. Roccaro, *Ind. Eng. Chem. Res.* **2023**, *62*, 10813–10827.
[5] B. H. R. Suryanto, H. L. Du, D. Wang, J. Chen, A. N. Simonov, D. R. MacFarlane, *Nat. Catal.* **2019**, *2*, 290–296.
[6] X. Fu, J. Zhang, Y. Kang, *Chem. Catal.* **2022**, *2*, 2590–2613.
[7] S. Z. Andersen, V. Čolić, S. Yang, J. A. Schwalbe, A. C. Nielander, J. M. McEnaney, K. Enemark-Rasmussen, J. G. Baker, A. R. Singh, B. A. Rohr,

M. J. Statt, S. J. Blair, S. Mezzavilla, J. Kibsgaard, P. C. K. Vesborg, M. Cargnello, S. F. Bent, T. F. Jaramillo, I. E. L. Stephens, J. K. Nørskov, I. Chorkendorff, *Nature* **2019**, *570*, 504–508.
[8] K. Li, S. Z. Andersen, A. Xu, N. H. Deissler, J. Bjarke, V. Mygind, C. Wei, *Science* **2023**, *712*, 707–712.
[9] T. Mou, J. Long, T. Frauenheim, J. Xiao, *ChemPlusChem* **2021**, *86*, 1211–1224.
[10] R. Chauhan, V. C. Srivastava, *Chem. Eng. J.* **2020**, *386*, 122065.
[11] H. Xu, Y. Ma, J. Chen, W. X. Zhang, J. Yang, *Chem. Soc. Rev.* **2022**, *51*, 2710–2758.
[12] X. Zhang, Y. Wang, Y. Wang, Y. Guo, X. Xie, Y. Yu, B. Zhang, *Chem. Commun.* **2022**, *58*, 2777–2787.
[13] H. Liu, J. Park, Y. Chen, Y. Qiu, Y. Cheng, K. Srivastava, S. Gu, B. H. Shanks, L. T. Roling, W. Li, *ACS Catal.* **2021**, *11*, 8431–8442.
[14] Y. Yao, S. Zhu, H. Wang, H. Li, M. Shao, *Angew. Chem., Int. Ed.* **2020**, *59*, 10479–10483.
[15] J. Li, G. Zhan, J. Yang, F. Quan, C. Mao, Y. Liu, B. Wang, F. Lei, L. Li, A. W. M. Chan, L. Xu, Y. Shi, Y. Du, W. Hao, P. K. Wong, J. Wang, S. X. Dou, L. Zhang, J. C. Yu, *J. Am. Chem. Soc.* **2020**, *142*, 7036–7046.
[16] J. Yuan, Z. Xing, Y. Tang, C. Liu, *ACS Appl. Mater. Interfaces* **2021**, *13*, 52469–52478.
[17] Y. Wang, W. Zhou, R. Jia, Y. Yu, B. Zhang, *Angew. Chem., Int. Ed.* **2020**, *59*, 5350–5354.
[18] J. X. Liu, D. Richards, N. Singh, B. R. Goldsmith, *ACS Catal.* **2019**, *9*, 7052–7064.
[19] Y. Bu, C. Wang, W. Zhang, X. Yang, J. Ding, G. Gao, *Angew. Chem., Int. Ed.* **2023**, *62*, e202217337.
[20] K. H. Kim, H. Lee, X. Huang, J. H. Choi, C. Chen, J. K. Kang, D. O'Hare, *Energy Environ. Sci.* **2023**, *16*, 663–672.
[21] B. Bi, A. Q. Dong, M. M. Shi, X. F. Sun, H. R. Li, X. Kang, R. Gao, Z. Meng, Z. Y. Chen, T. W. Xu, J. M. Yan, Q. Jiang, *Small Struct.* **2023**, *4*, 2200308.
[22] Y. Wang, A. Xu, Z. Wang, L. Huang, J. Li, F. Li, J. Wicks, M. Luo, D. H. Nam, C. S. Tan, Y. Ding, J. Wu, Y. Lum, C. T. Dinh, D. Sinton, G. Zheng, E. H. Sargent, *J. Am. Chem. Soc.* **2020**, *142*, 5702–5708.
[23] H. Li, C. Yan, H. Guo, K. Shin, S. M. Humphrey, C. J. Werth, G. Henkelman, *ACS Catal.* **2020**, *10*, 7915–7921.
[24] K. Chen, Z. Ma, X. Li, J. Kang, D. Ma, K. Chu, *Adv. Funct. Mater.* **2023**, *33*, 2209890.
[25] H. Liu, X. Lang, C. Zhu, J. Timoshenko, M. Rüscher, L. Bai, N. Guijarro, H. Yin, Y. Peng, J. Li, Z. Liu, W. Wang, B. R. Cuenya, J. Luo, *Angew. Chem., Int. Ed.* **2022**, *61*, e202202556.
[26] X. Lu, H. Song, J. Cai, S. Lu, *Electrochem. Commun.* **2021**, *129*, 107094.
[27] D. Qin, S. Song, Y. Liu, K. Wang, B. Yang, S. Zhang, *Angew. Chem., Int. Ed.* **2023**, *62*, e202304935.
[28] R. Daiyan, T. Tran-Phu, P. Kumar, K. Iputera, Z. Tong, J. Leverett, M. H. A. Khan, A. Asghar Esmailpour, A. Jalili, M. Lim, A. Tricoli, R. S. Liu, X. Lu, E. Lovell, R. Amal, *Energy Environ. Sci.* **2021**, *14*, 3588–3598.
[29] J. Li, J. Gao, T. Feng, H. H. Zhang, D. Liu, C. Zhang, S. Huang, C. Wang, F. Du, C. Li, C. Guo, *J. Power Sources* **2021**, *511*, 230463.
[30] Z. Song, Y. Liu, Y. Zhong, Q. Guo, J. Zeng, Z. Geng, *Adv. Mater.* **2022**, *34*, 2204306.
[31] H. Jiang, G. F. Chen, O. Savateev, J. Xue, L. X. Ding, Z. Liang, M. Antonietti, H. Wang, *Angew. Chem., Int. Ed.* **2023**, *62*, e202218717.
[32] J. Yang, H. Qi, A. Li, X. Liu, X. Yang, S. Zhang, Q. Zhao, Q. Jiang, Y. Su, L. Zhang, J. F. Li, Z. Q. Tian, W. Liu, A. Wang, T. Zhang, *J. Am. Chem. Soc.* **2022**, *144*, 12062–12071.
[33] Q. Chen, X. An, Q. Liu, X. Wu, L. Xie, J. Zhang, W. Yao, M. S. Hamdy, Q. Kong, X. Sun, *Chem. Commun.* **2022**, *58*, 517–520.
[34] F. Chen, Z. Wu, S. Gupta, D. J. Rivera, S. V. Lambeets, S. Pecaut, J. Yoon, T. Kim, P. Zhu, Y. Z. Finfrock, D. M. Meira, G. King, G. Gao, W. Xu, D. A. Cullen, H. Zhou, Y. Han, D. E. Perea, C. L. Muhich, H. Wang, *Nat. Nanotechnol.* **2022**, *17*, 759–767.
[35] J. Y. Fang, Q. Z. Zheng, Y. Y. Lou, K. M. Zhao, S. N. Hu, G. Li, O. Akdim, X. Y. Huang, S. G. Sun, *Nat. Commun.* **2022**, *13*, 7899.
[36] N. Q. Tran, L. T. Duy, D. C. Truong, B. T. Nguyen Le, B. T. Phan, Y. Cho, X. Liu, H. Lee, *Chem. Commun.* **2022**, *58*, 5257–5260.
[37] R. Redón, A. Herrera-gomez, N. G. García-pe, A. L. Fernández-osorio, M. Bravo-sanchez, G. Gomez-sosa, *Appl. Surf. Sci.* **2015**, *340*, 25–34.
[38] A. C. Miller, G. W. Simmons, *Surf. Sci. Spec.* **1993**, *2*, 55–60.
[39] D. Li, G. Wang, L. Cheng, C. Wang, X. Mei, *ACS Omega* **2018**, *3*, 14755–14765.
[40] Y. Liang, R. Zhang, K. Xiao, F. Ye, X. Ma, W. Liu, H. Yin, B. Mao, X. Song, C. Hu, *Chem. Commun.* **2024**, *60*, 4699–4702.
[41] V. Hayez, A. Franquet, A. Hubin, H. Terryn, *Surf. Interface Anal.* **2004**, *36*, 876–879.
[42] D. J. Morgan, *Surf. Interface Anal.* **2015**, *47*, 1072–1079.
[43] M. Pang, Y. Fang, L. Chen, R. Sun, X. Li, H. Pang, S. Zhang, L. Xu, D. Sun, Y. Tang, *Nanoscale* **2024**, *16*, 17519–17526.
[44] Y. Wang, A. Dutta, A. Iarchuk, C. Sun, S. Vesztergom, P. Broekmann, *ACS Catal.* **2023**, *13*, 8169–8182.
[45] A. Paliwal, C. D. Bandas, E. S. Thornburg, R. T. Haasch, A. A. Gewirth, *ACS Catal.* **2023**, *13*, 6754–6762.
[46] H. Liu, X. Lang, C. Zhu, J. Timoshenko, M. Rüscher, L. Bai, N. Guijarro, H. Yin, Y. Peng, J. Li, Z. Liu, W. Wang, B. R. Cuenya, J. Luo, *Angew. Chem., Int. Ed.* **2022**, *61*, e202202556.
[47] P. Nagaraja, M. Shivaswamy, H. Kumar, *Int. J. Environ. Anal. Chem.* **2001**, *80*, 39–48.
[48] Z. Bi, J. Hu, M. Xu, H. Zhang, Y. Zhou, G. Hu, *Angew. Chem., Int. Ed.* **2024**, *63*, e202313434.
[49] S. Liu, Y. Zhao, Z. Chen, D. Gao, F. Feng, T. Rios-Studer, J. Bansmann, J. Biskupek, U. Kaiser, R. Liu, C. Streb, *ChemElectroChem* **2024**, *11*, e202400291.

Manuscript received: October 02, 2024
Revised manuscript received: December 09, 2024
Accepted manuscript online: December 19, 2024
Version of record online: January 10, 2025